JACS
JOURNAL OF THE AMERICAN CHEMICAL SOCIETY
pubs.acs.org/JACS
Article

Visualizing Light-Induced Microstrain and Phase Transition in Lead-Free Perovskites Using Time-Resolved X-Ray Diffraction

Yingqi Wang,○ Cunming Liu,○ Yang Ren, Xiaobing Zuo, Sophie E. Canton, Kaibo Zheng, Kuangda Lu, Xujie Lü, Wenge Yang,* and Xiaoyi Zhang*

Cite This: J. Am. Chem. Soc. 2022, 144, 5335−5341

ABSTRACT: Metal halide perovskites have emerged as promising materials for optoelectronic applications in the last decade. A large amount of effort has been made to investigate the interplay between the crystalline lattice and photoexcited charge carriers as it is vital to their optoelectronic performance. Among them, ultrafast laser spectroscopy has been intensively utilized to explore the charge carrier dynamics of perovskites, from which the local structural information can only be extracted indirectly. Here, we have applied a time-resolved X-ray diffraction technique to investigate the structural dynamics of prototypical two-dimensional lead-free halide perovskite $Cs_3Bi_2Br_9$ nanoparticles across temporal scales from 80 ps to microseconds. We observed a quick recoverable (a few ns) photoinduced microstrain up to 0.15% and a long existing lattice expansion (~a few hundred nanoseconds) at mild laser fluence. Once the laser flux exceeds 1.4 mJ/cm^2, the microstrain saturates and the crystalline phase partially transfers into a disordered phase. This photoinduced transient structural change can recover within the nanosecond time scale. These results indicate that photoexcitation of charge carriers couples with lattice distortion, which fundamentally affects the dielectric environment and charge carrier transport.

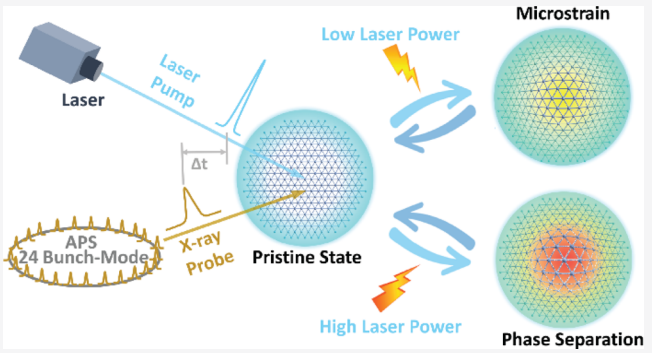

INTRODUCTION

Metal halide perovskites have recently attracted increasing attention with their superior photovoltaic and optoelectronic properties. Perovskite solar cells have gone through an explosive increase in power conversion efficiency from 3.8 to over 25% in the last decade.[1,2] They have also been extensively explored for the applications of light-emitting diodes and lasers because of their outstanding emission properties.[3−5] Although significant progress has been made in device efficiency,[6] the fundamental understanding of their photoinduced structural dynamics, which is directly linked to their performance and stability, is largely underexplored.

The strongly polar and soft fluctuating nature of the metal halide perovskite lattice gives rise to interesting structure−property relationships.[7−10] Structural rearrangement readily occurs under external stimulation or perturbation, such as photoexcitation, because of lattice softness.[11−16] This is in contrast to classical inorganic semiconductors whose atomic displacement is usually small under similar conditions.[17,18] The dynamic lattice response directly contributes to the dielectric environment experienced by charge carriers in metal halide perovskites and, therefore, influences their properties such as exciton binding strength, charge carrier mobility, and recombination rate. Thus, directly unveiling the structural dynamics upon photoexcitation is indispensable for fundamentally understanding the optoelectronic behavior in these perovskite materials.

Time-resolved optical techniques, such as ultrafast Raman, infrared, terahertz, and visible light spectroscopy, have revealed valuable information on transient phonon and electronic structures of metal halide perovskites upon photoexcitation.[8,19,20] Although optical measurements can probe dipole-allowed electronic transitions with high time resolution, they only indirectly probe the atomic positions and cannot resolve optical dark states as well as the long-range order of the lattice structure. Recently, emerging ultrafast X-ray and electron scattering techniques have enabled us to directly reveal structural dynamic information of materials upon photoexcitation. Pioneering work applying ultrafast electron or X-ray scattering on lead halide perovskites has revealed light-induced phase transitions[21] or rotational disordering of the Pb-Br octahedron,[22] and a very recent study analyzed the structural distortion with spherical polaronic local strain field.[23] The

Received: November 7, 2021
Published: March 18, 2022

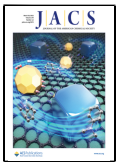

https://doi.org/10.1021/jacs.1c11747
J. Am. Chem. Soc. 2022, 144, 5335−5341

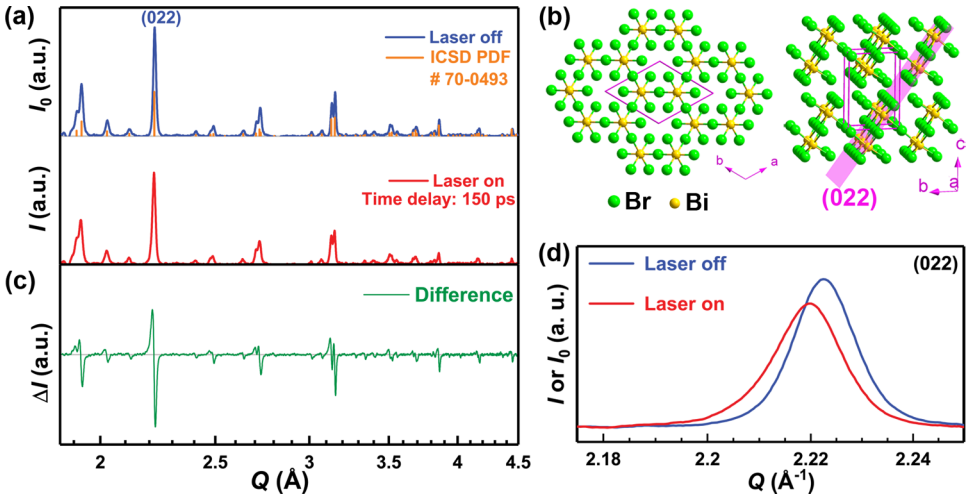

Figure 1. (a) XRD patterns of the $Cs_3Bi_2Br_9$ nanocrystal (NC) suspension before (laser off) and at 150 ps after (laser on) the photoexcitation, which are compared to the standard pattern of the $Cs_3Bi_2Br_9$ (ICSD PDF# 70-0493). (b) Crystal structure of $Cs_3Bi_2Br_9$ with the trigonal *P*-3*m*1 space group, viewed from the directions parallel and perpendicular to the $[Bi_2Br_9]^{3-}$ layer. (c) Difference of XRD patterns at a time delay of 150 ps with a pulse energy density of 0.6 mJ/cm^2 ($\Delta I = I$(laser on) $- I_0$(laser off)). (d) Comparison of the (0 2 2) diffraction peak before and at 150 ps after laser photoexcitation.

structural variation in lead-free perovskite is different from that in the lead-containing one. Recent transient X-ray absorption spectroscopy results suggest the formation of a halide dimer (V_k center) under photoexcitation in bismuth halide perovskite.[24] However, the impact of structural distortion on a long-range order still needs in-depth inspection. Such information is vital for understanding the phonon−carrier interaction and phase stability which directly impacts carrier lifetime and device performance.

Here, we employed ultrafast laser-initiated time-resolved X-ray diffraction (TR-XRD) (with a time resolution of 79 ps) to directly track the structural evolution of a prototypical two-dimensional (2D) lead-free perovskite ($Cs_3Bi_2Br_9$) upon photoexcitation. Light-induced microstrain up to 0.15% emerges with laser power as low as 0.6 mJ/cm^2, concurrently with a lattice expansion. The microstrain relaxes within 10 ns while the full recovery of lattice expansion takes hundreds of nanoseconds. When the laser excitation flux exceeds 1.4 mJ/cm^2, microstrain does not further increase, but a secondary disordered phase appears. Both the observed microstrain and phase boundary would increase the scattering and recombination probability of the photogenerated carriers, thus impairing the performance. Solving this problem in the design and development of lead-free perovskites could help enhance their performance and stability.

RESULTS AND DISCUSSION

TR-XRD Patterns under Moderate Laser Excitation Power. $Cs_3Bi_2Br_9$ NCs were synthesized by a modified ligand-assisted precipitation method[25] and then dispersed in toluene. Figure S1a shows the transmission electron microscopy (TEM) images of the as-synthesized NCs, The $Cs_3Bi_2Br_9$ nanoparticles are hexagonal plate NCs with an average lateral diameter of 80 nm (Figure S1b). The thickness of the nanoplates is estimated to be ∼20 nm from vertically oriented flakes in the TEM images. TR-XRD experiments were performed at the Advanced Photon Source 11-ID-D of the Argonne National Laboratory. A 400 nm, 110 fs (full-width full maximum (FWHM)) laser "pump" pulse was used to create band-gap excitation of the NCs followed by 79 ps (FWHM) X-ray "probe" pulses at certain time delays to monitor the structural changes *via* collecting the X-ray scattering signals (Figure S3). The 400 nm laser is selected, which is just over the exciton peak (∼432 nm, Figure S4), to minimize the undesired thermal and hot carrier effect. The details of the experimental setup can be found in the Supporting Information (SI). Figure 1a shows the static XRD pattern of the $Cs_3Bi_2Br_9$ NC liquid suspension with the scattering contribution from the pure solvent been subtracted. $Cs_3Bi_2Br_9$ (space group $P\bar{3}m1$) is a vacancy-ordered 2D perovskite, formed by corrugated layers of corner-sharing $BiBr_6$ octahedra (Figure 1b). The position and intensity of diffraction peaks of $Cs_3Bi_2Br_9$ NCs match well with those from the calculated XRD pattern of the bulk single crystal (ICSD PDF # 70-0493, Figure 1a). This indicates that NCs retain good crystallinity and purity. The strongest diffraction at Q (scattering vector) of 2.22 Å^{-1} comes from the (022) crystal plane (Figure 1b).

Figure 1c shows a typical difference spectrum between the XRD data before and at 150 ps after laser excitation with a flux of 0.6 mJ/cm^2. All diffraction peaks show similar behavior upon photoexcitation, with asymmetric intensity reduction in the higher Q range and increased intensity in the lower Q range. When zooming into the strongest (022) diffraction peak (Figure 1d), we can clearly observe its shift toward smaller Q and broadening after laser excitation. The data analysis based on the PVII peak function (details in the SI) reveals a 16% reduction in the peak height and 14% increase in the peak width.

Previous studies have shown that when a semiconducting thin film or metal nanoparticle is excited by photons with energy much larger than its band gap (generating the so-called "hot carriers"), the diffraction peak intensity changes due to the laser heating effect can be well described using the Debye−Waller (DW) model.[22,26,27] Here, we apply this model to check whether the observed peak broadening and intensity attenuation after photoexcitation are caused by a similar effect:

$$A(Q, t) \propto \exp\left(-\frac{1}{3}Q^2 < u^2(t) >\right) \quad (1)$$

https://doi.org/10.1021/jacs.1c11747
J. Am. Chem. Soc. 2022, 144, 5335−5341

where $A(Q, t)$ is the time-dependent integrated peak intensity at the scattering vector Q, $\langle u^2(t)\rangle$ is the mean-square displacement of the photoexcited atoms averaged spatially over the sample, and $\exp(-Q^2\langle u^2\rangle/3)$ is denoted as the DW factor or temperature factor. If the thermal effect is dominant, that is, the peak evolution follows the DW model, $-\ln(A/A_0)$ will be proportional to Q^2 (A_0 is the integrated intensity before photoexcitation). We fitted the diffraction patterns with a sum of multiple PVII peak functions to obtain peak parameters (Figure 2a). As shown in Figure 2b, the $-\ln(A/A_0)$ is almost

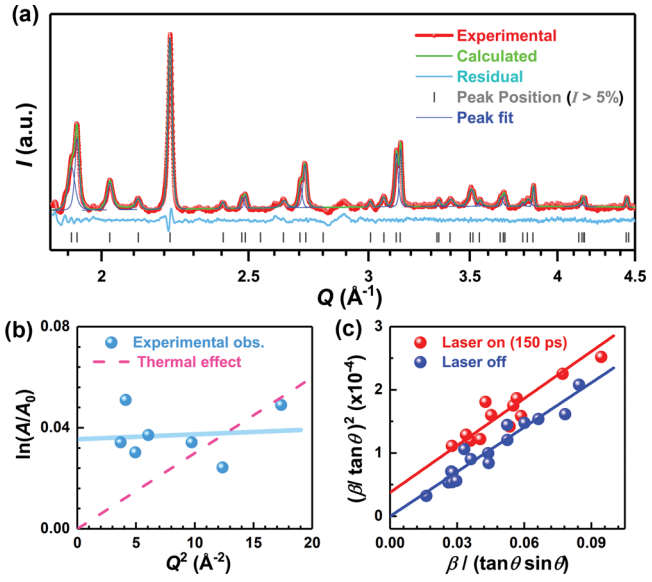

Figure 2. Peak analysis of the $Cs_3Bi_2Br_9$ diffraction pattern at 150 ps after laser excitation (400 nm, 0.6 mJ/cm^2). (a) Peak decomposition by profile fitting using the PVII peak function (red: experimental data, green: calculated fitting including all fitted peaks; light gray: calculated Bragg peak position; blue: fitted peaks; cyan: fitting residual). (b) Semilog plot of intensity change as a function of the squared scattering factor Q^2 (light blue line: guide for the eye), which is compared to the one deviated from the DW model (dashed pink line). (c) Linear fitting of integral-breadth analysis using Halder–Wagner plots before and at 150 ps after laser excitation, where the increase of intercept indicates rising microstrain after photoexcitation.

constant on Q^2 ranging from 4 to 18 (light blue line and scatters), which is different from the one predicted by the DW model reflecting a pure thermal expansion trend (dashed pink line). This implies that the thermal effect from laser heating is not the dominant cause of peak intensity change in our studies. Actually, our band-gap photoexcitation should produce mostly cold charge carriers, which could not contribute a large lattice heating effect.[22,28]

Two other possible explanations of peak broadening are the changes in strain distribution or the coherent domain size of diffraction.[29] These two factors follow different dependences over the diffraction vector, which allows separating the cause of peak broadening over a wide 2θ range. Detailed structural analysis of the observed diffraction data was performed using the Halder–Wagner equation[29,30] to further examine the origin of the peak broadening:

$$\left(\frac{\beta}{\tan\theta}\right)^2 = \frac{K\lambda}{D}\cdot\frac{\beta}{\tan\theta\,\sin\theta} + 16\varepsilon^2 \qquad (2)$$

Here, the integral breadth β is defined as the peak area divided by the peak height, D is the coherent crystal domain size, ε is the microstrain, K is a dimensionless shape factor, and λ is the X-ray wavelength (1.0589 Å). Figure 2c shows the Halder–Wagner plot of $Cs_3Bi_2Br_9$ NCs before and at 150 ps after laser excitation. The slope and y intercept from the linear fitting correspond to $K\lambda/D$ and $16\varepsilon^2$, respectively. Before laser excitation, the strain in the NCs was close to zero. After laser excitation, the fitted line shifts upward while the slope remained unchanged, suggesting an increase in the microstrain without changes in the domain size. The crystal domain size D is calculated to be ~54 nm from the fitted slope, while the increase in crystal strain ε is ~0.15% from the y intercept.

We examined the microscopic scenario to understand the origin of the microstrain increase. Because of the highly deformable and polar nature of the metal halide framework, they are prone to lattice relaxation after electronic excitation.[31,32] This is in contrast to classical crystalline semiconductors in which delocalized electronic states act as Bloch waves and are comparably insensitive to local lattice dynamics.[8,19] Time-resolved optical spectroscopy experiments indicate local geometrical distortion upon photoexcitation.[8,19,33,34] Ultrafast electronic diffraction and X-ray absorption suggest that the local distortion could be rotational disorder of the halide octahedra, possibly forming small polaron in the configuration halide dimer.[22,24] It is proposed that this geometry distortion is driven by the vibrational wave packet in the electronically excited state,[8,34] and it completes in 90 fs, which is much faster than the traditional thermal effect.[35] In lead halide perovskite, the lattice deformation forms large polarons, which have been proposed to screen the Coulombic potential and protect charge carriers from scattering.[3,9] In lead free halide perovskite, there are more reports on small polaron formation from the charge–lattice interaction.[32,36] For example, the self-trapped state is believed to be responsible for the broad photoluminescence emission in $Cs_3M_2I_9$ (M = Bi, Sb).[37] Upon photoexcitation, the formation of the V_k center (Br_2^- dimer)[24] in $Cs_3Bi_2Br_9$ produces an internal electrical field, leading to anomalies in photoconductivity.[38] Here, we visualize the increase of microstrain in photoexcited $Cs_3Bi_2Br_9$, which should be a long-range integration of the local distortions. The microstrain could have potential impact on photostability and migration of charge carriers.

TR-XRD Kinetics under Moderate Laser Excitation Fluence. Figure 3a shows the difference between the diffraction patterns before and after laser excitation (0.6 mJ/cm^2) at various delays from 150 ps to 4 μs. Figure 3b is a zoomed-in view of the strongest (022) diffraction peak. Recovery kinetics of the peak height and peak width are similar (Figure 3c top panel), revealing two exponential time components: τ_1 = 1.3 ± 0.2 ns (72%) and τ_2 = 9 ± 4 ns (28%) (see the fitting details in the SI). The kinetic trace of the photoinduced microstrain (Figure 3c, bottom panel) can be fitted well with a single exponential decay of τ = 1.5 ± 0.3 ns, which is consistent with the dominant fast lifetime component (1.3 ns) in the peak height and peak width kinetics. However, the longer one (9 ns) is missing in the microstrain kinetics. This might be because that the microstrain extracted based on eq 2 has larger uncertainties than that can be resolved from the width or height of the strongest peak. The contribution of the minor lifetime component is too small to be detected in microstrain kinetics. Importantly, the lifetimes of ~1 ns and ~9 ns are comparable to the lifetime in the reported PL and OTA

https://doi.org/10.1021/jacs.1c11747
J. Am. Chem. Soc. 2022, 144, 5335–5341

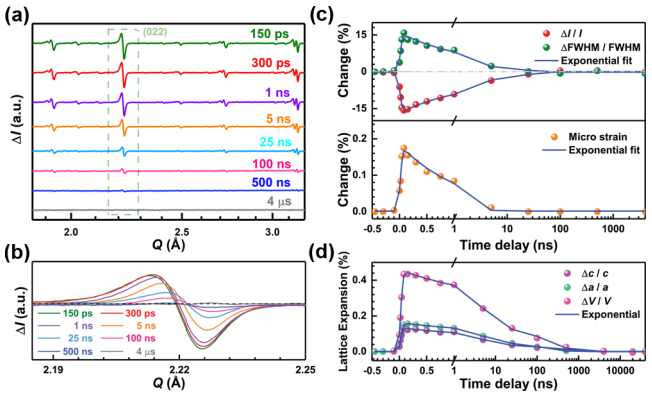

Figure 3. Time-resolved analysis of diffraction data under 400 nm excitation at 0.6 mJ/cm^2. (a) Differential diffraction pattern at time delays from t = 150 ps to 4 μs. (b) Zoom in of the differential data at the (0 2 2) plane (green rectangle in Figure 1a). (c) Time-dependent evolution for the changes in intensity and *FWHM* of the (0 2 2) peak (top panel) as well as microstrain (bottom panel). (d) Time-dependent evolution of lattice expansion examined from the lattice constants a and c and the cell volume V.

measurements of $Cs_3Bi_2Br_9$,[25,39] suggesting that this structural dynamic component originates from photogenerated excitons.

In Figure 3a,b, the negative shift of the diffraction peak position (ΔQ) indicates a lattice expansion taking in place. The kinetics of the Q shift are displayed in Figure 3d. To further understand the photoinduced lattice expansion, we also studied the evolutions of $\Delta a/a$, $\Delta c/c$, and $\Delta V/V$, which are the relative changes of unit cell parameters (Figure 3d). Here, a, c, and V were generated from the Le Bail refinement using space group P-3m (164) and the PVII peak function. The kinetics of $\Delta a/a$, $\Delta c/c$, and $\Delta V/V$ can be globally fitted using the three-exponential decay function in which the two short lifetime components (τ_1 = 1.3 ns and τ_2 = 9 ns) are adapted from the kinetics fitting of peak intensity and width changes, plus a long lifetime component of 202 ± 32 ns (Figure 3d). The common lifetime components indicate that the NC has homogeneous lattice expansion. The photogenerated electrons in the conduction band can populate antibonding states, whereas the holes in the valence band vacate the bonding states, thus, leading to weakening and elongation of the Bi−Br bonds.[29] It should be pointed out that the photoinduced unit cell expansion here is distinct from the thermal effect. The NC is surrounded by a solvent kept at 18 °C (experimental details in SI). Assuming that all the absorbed photon energy converts to heat in the NCs, this would only cause an average 22 °C rise in temperature and ~0.22% increase in cell volume at most, much smaller than the 0.43% cell volume expansion we observed (calculation detailed in the SI). In addition, the change of the diffraction peak does not follow the heat-induced model of Debye−Waller dependence as discussed previously. Therefore, the observed lattice kinetics does not come solely from thermal expansion, but also from light-induced lattice expansion and microstrain. The small portion of long-lived state ~200 ns might originate from the nonradiative recombination of photoinduced charge carriers localized at some trapping states; the lack of this long-lived state in the peak width and peak height also indicates that it is not a thermal state.

TR-XRD under Elevated Laser Excitation Fluence. Figure S7 shows the fluence dependence of the differential TR-XRD signal at 300 ps after photoexcitation. By increasing the laser power, the increasing negative peak on the right side indicates enhanced crystal distortion and loss of peak intensity. Under the low fluence of 0.6 mJ/cm^2, the sharp positive peak comes from the lattice expansion and shift of the diffraction peak toward lower Q. The left side of the positive peak broadened significantly under higher fluence (≥1.4 mJ/cm^2), suggesting the formation of a disordered phase with larger lattice parameters. The corresponding (022) peak could be fitted with a main peak and a broader side peak at lower Q. It is worth noting that with the increase of excitation fluence from 1.4 to 5.1 mJ/cm^2, the position of the light-induced broad side peak remains constant (Figure 4a), suggesting that a

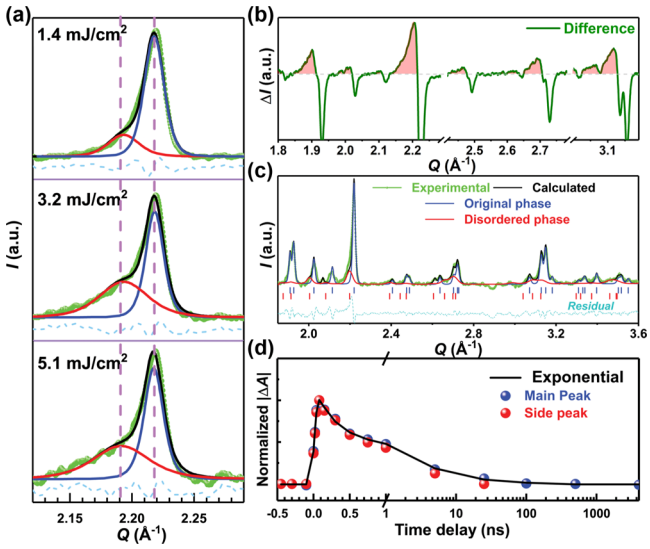

Figure 4. (a) Laser power dependence analysis of diffraction peaks at 150 ps after photoexcitation. Fitting of the (0 2 2) peak and the emerged side peak representing the second disordered phase under different laser powers. With increasing fluence, the position of the side peak remains constant. (b, c) Analysis of time-resolved diffraction data at 150 ps time delay with a laser fluence of 1.4 mJ/cm^2. (b) Red shadow for the second disordered phase in the differential diffraction spectra. (c) Set of side peaks (red line) with broader *FWHM* emerges on the left side of the original crystalline phase (blue line). (d) Time-dependent integrated area changes for the (0 2 2) main peak and its side peak.

metastable state with larger lattice parameters might be produced. Similar analysis was applied to the full range, as shown in Figure 4b,c, and a set of side peaks with a broader *FWHM* emerge clearly on the left side of the original crystalline phase. The integrated area change of the main peak and side peak around 2.21 Å^{-1} are shown in Figure 4d. Because the decay of the disordered phase correlates with the recovery of the original phase, the integration area changes of both peaks are fitted with the same double-exponential decay function, revealing two lifetime components 0.25 ± 0.05 and 3.2 ± 0.7 ns, respectively. Structural modification of the crystallinity state by the ultrafast pulse laser has been reported before. A metastable transient phase of 1T-TaS_2 is triggered by an infrared laser with an optical doping effect.[40] A study on photoexcited VO_2 has attributed the formation of an ultrafast disordered phase by transiently modifying the interatomic potential and the atomic positions.[41] We examined the microstrain condition in the main phase by the Halder−Wagner plot, the same approach used for the analysis of the 0.6

https://doi.org/10.1021/jacs.1c11747
J. Am. Chem. Soc. 2022, 144, 5335−5341

mJ/cm^2 excitation data (Figure S8). Despite the twofold increase in the excitation fluence, the photoinduced microstrain in the main phase remained almost unchanged. The microstrain shows saturation at relatively low laser fluence, while the secondary phase keeps growing with increasing fluence. The formation of the secondary disordered phase could be the channel that releases excessive microstrain from the main phase.

It is interesting to compare the recently uncovered structural dynamics of 3D lead halide perovskite $CsPbBr_3$ with our findings in the 2D lead-free halide perovskite $Cs_3Bi_2Br_9$. $CsPbBr_3$ is a typical lead halide perovskite where $PbBr_6$ octahedra connect to each other in a 3D network. Under the photoexcitation, its NC undergoes an orthorhombic-to-cubic crystalline phase transition which recovers in 510 ps, and no microstrain is observed. Two possible reasons can be ascribed to the differences between $CsPbBr_3$ and $Cs_3Bi_2Br_9$. First, from the phase diagram and phase transition point of view, $CsPbBr_3$ has three phases (cubic, tetragonal, and orthorhombic) near room temperature with similar potential energies, and the phase transitions occur within a small temperature range of 130 °C.[42] The photostimulation could bring in enough energy to drive the phase transitions in this system.[43] The light-induced local structural distortion or microstrain, if there were any, could be released by crystalline phase transformation. In contrast, the trigonal phase of $Cs_3Bi_2Br_9$ is stable from room temperature to 460 °C (Figure S5). The photoinduced microstrain cannot be released through the phase transition in $Cs_3Bi_2Br_9$ NCs. Second, compared to the $CsPbBr_3$ with a 3D lattice framework, $Cs_3Bi_2Br_9$ in this study has a 2D layer crystalline structure, in which the metal-halide layers are separated by dielectric alkali ions, giving rise to dielectric confinement. The photogenerated charge carriers are more localized and have higher exciton binding energy because of quantum confinement compared to 3D perovskite.[44,45] The localized excitons couple more strongly with the lattice in low dimensional perovskites so that the self-trap state is widely observed in these materials.[37] Thus, the local structural distortion from photoinduced excitons/polarons may lead to an observable increase of microstrain in $Cs_3Bi_2Br_9$.

The structural dynamics of the halide perovskite studied here is intrinsically correlated with the material's properties. The microstrain arises from inhomogeneous variations of the crystal lattice that will increase charge carrier scattering, which is directly associated with nonradiative recombination loss.[46] When the secondary disordered phase emerges under higher excitation fluence, the phase boundary will further increase the carrier scattering and nonradiative loss. Therefore, learning how to reduce and even eliminate the microstrain and secondary phase under light illumination through the design of perovskites is critical for advancing their optoelectronic properties.

CONCLUSIONS

In summary, the light-induced structural dynamics of a prototypical 2D lead-free perovskite ($Cs_3Bi_2Br_9$) were systematically investigated using time-resolved XRD. Under a low excitation fluence of 0.6 mJ/cm^2, an increase of microstrain was discovered in the NCs because of light-induced local distortion and lattice expansion. As the excitation fluence exceeded 1.4 mJ/cm^2, a light-induced disordered phase was observed after photoexcitation to release the excessive strain. The light-induced strain and disorder phase in $Cs_3Bi_2Br_9$ recovered in the nanosecond time scale. The photoinduced macrostrain and metastable disordered phases influence the scattering of charge carriers and their dynamics, which may further impact the material properties. In comparison with the recent TR-XRD study, where 3D $CsPbBr_3$ NCs underwent a phase transition upon excitation, the different structural response to release photoinduced strains is probably attributed to the confined 2D structure of $Cs_3Bi_2Br_9$.

ASSOCIATED CONTENT

Supporting Information

The Supporting Information is available free of charge at https://pubs.acs.org/doi/10.1021/jacs.1c11747.

Experimental details, data analysis details, estimation of the heating effect, schematic setup of TR-XRD, optical absorption spectrum, in situ XRD pattern upon heating, lattice expansion under increasing temperature, differential diffraction intensity at 300 ps after excitation, and integral-breadth analysis at elevated power density (PDF)

AUTHOR INFORMATION

Corresponding Authors

Wenge Yang − *Center for High Pressure Science & Technology Advanced Research, Pudong, Shanghai 201203, China*; Email: yangwg@hpstar.ac.cn

Xiaoyi Zhang − *X-ray Science Division, Argonne National Laboratory, Lemont, Illinois 60439, United States*; orcid.org/0000-0001-9732-1449; Email: xyzhang@anl.gov

Authors

Yingqi Wang − *Center for High Pressure Science & Technology Advanced Research, Pudong, Shanghai 201203, China*; Present Address: Department of Physics, University of Washington, Seattle, Washington 98195, United States; orcid.org/0000-0002-9556-5623

Cunming Liu − *X-ray Science Division, Argonne National Laboratory, Lemont, Illinois 60439, United States*

Yang Ren − *Department of Physics, City University of Hong Kong, Kowloon 999077, Hong Kong, China*; orcid.org/0000-0001-9831-6035

Xiaobing Zuo − *X-ray Science Division, Argonne National Laboratory, Lemont, Illinois 60439, United States*

Sophie E. Canton − *European XFEL, 22869 Schenefeld, Germany*; orcid.org/0000-0003-4337-8129

Kaibo Zheng − *Department of Chemical Physics and Nanolund, Lund University, 22100 Lund, Sweden*; orcid.org/0000-0002-7236-1070

Kuangda Lu − *Biomedical Engineering Department, Peking University, Beijing 100871, China*

Xujie Lü − *Center for High Pressure Science & Technology Advanced Research, Pudong, Shanghai 201203, China*; orcid.org/0000-0001-8402-7160

Complete contact information is available at: https://pubs.acs.org/10.1021/jacs.1c11747

Author Contributions

○Y.W. and C.L. contributed equally.

Notes

The authors declare no competing financial interest.

https://doi.org/10.1021/jacs.1c11747
J. Am. Chem. Soc. 2022, 144, 5335−5341

■ ACKNOWLEDGMENTS

Wang is supported by Science Challenge Project No. TZ2016001, China Scholarship Council and the National Nature Science Foundation of China (NSFC) (Grant Nos. 51527801 and U1930401). Liu, Zuo and Zhang are supported by the DOE Office of Science by Argonne National Laboratory under Contract No. DE-AC02-06CH11357. This research used resources of the Advanced Photon Source; a U.S. Department of Energy (DOE) Office of Science User Facility operated for the DOE Office of Science by Argonne National Laboratory under Contract No. DE-AC02-06CH11357.

■ REFERENCES

(1) Snaith, H. J. Present status and future prospects of perovskite photovoltaics. *Nat. Mater.* **2018**, *17*, 372−376.
(2) Best Cell-Efficiency Chart (NREL, accessed September 2021); https://www.nrel.gov/pv/assets/pdfs/best-research-cell-efficiencies-rev210726.pdf.
(3) Fu, Y.; Zhu, H.; Chen, J.; Hautzinger, M. P.; Zhu, X. Y.; Jin, S. Metal halide perovskite nanostructures for optoelectronic applications and the study of physical properties. *Nat. Rev. Mater.* **2019**, *4*, 169−188.
(4) Schlaus, A. P.; Spencer, M. S.; Miyata, K.; Liu, F.; Wang, X.; Datta, I.; Lipson, M.; Pan, A.; Zhu, X. Y. How lasing happens in CsPbBr3 perovskite nanowires. *Nat. Commun.* **2019**, *10*, 265.
(5) Jia, Y.; Kerner, R. A.; Grede, A. J.; Rand, B. P.; Giebink, N. C. Continuous-wave lasing in an organic−inorganic lead halide perovskite semiconductor. *Nat. Photonics* **2017**, *11*, 784−788.
(6) Zhao, D.; Wang, C.; Song, Z.; Yu, Y.; Chen, C.; Zhao, X.; Zhu, K.; Yan, Y. Four-Terminal All-Perovskite Tandem Solar Cells Achieving Power Conversion Efficiencies Exceeding 23%. *ACS Energy Lett.* **2018**, *3*, 305−306.
(7) Herz, L. M. Charge-carrier dynamics in organic-inorganic metal halide perovskites. *Annu. Rev. Phys. Chem.* **2016**, *67*, 65−89.
(8) Batignani, G.; Fumero, G.; Srimath Kandada, A. R.; Cerullo, G.; Gandini, M.; Ferrante, C.; Petrozza, A.; Scopigno, T. Probing femtosecond lattice displacement upon photo-carrier generation in lead halide perovskite. *Nat. Commun.* **2018**, *9*, 1971.
(9) Zhu, H.; Miyata, K.; Fu, Y.; Wang, J.; Joshi, P. P.; Niesner, D.; Williams, K. W.; Jin, S.; Zhu, X.-Y. Screening in crystalline liquids protects energetic carriers in hybrid perovskites. *Science* **2016**, *353*, 1409−1413.
(10) Miyata, K.; Meggiolaro, D.; Trinh, M. T.; Joshi, P. P.; Mosconi, E.; Jones, S. C.; De Angelis, F.; Zhu, X.-Y. Large polarons in lead halide perovskites. *Sci. Adv.* **2017**, *3*, No. e1701217.
(11) Fafarman, A. T. More stable when relaxed. *Nat. Energy* **2018**, *3*, 617.
(12) Saidaminov, M. I.; Kim, J.; Jain, A.; Quintero-Bermudez, R.; Tan, H.; Long, G.; Tan, F.; Johnston, A.; Zhao, Y.; Voznyy, O. Suppression of atomic vacancies via incorporation of isovalent small ions to increase the stability of halide perovskite solar cells in ambient air. *Nat. Energy* **2018**, *3*, 648.
(13) Cortecchia, D.; Neutzner, S.; Srimath Kandada, A. R.; Mosconi, E.; Meggiolaro, D.; De Angelis, F.; Soci, C.; Petrozza, A. Broadband emission in two-dimensional hybrid perovskites: The role of structural deformation. *J. Am. Chem. Soc.* **2017**, *139*, 39−42.
(14) Dohner, E. R.; Jaffe, A.; Bradshaw, L. R.; Karunadasa, H. I. Intrinsic white-light emission from layered hybrid perovskites. *J. Am. Chem. Soc.* **2014**, *136*, 13154−13157.
(15) Hu, T.; Smith, M. D.; Dohner, E. R.; Sher, M.-J.; Wu, X.; Trinh, M. T.; Fisher, A.; Corbett, J.; Zhu, X.-Y.; Karunadasa, H. I.; Lindenberg, A. M. Mechanism for broadband white-light emission from two-dimensional (110) hybrid perovskites. *J. Phys. Chem. Lett.* **2016**, *7*, 2258−2263.
(16) Smith, M. D.; Jaffe, A.; Dohner, E. R.; Lindenberg, A. M.; Karunadasa, H. I. Structural origins of broadband emission from layered Pb−Br hybrid perovskites. *Chem. Sci.* **2017**, *8*, 4497−4504.
(17) Katan, C.; Mohite, A. D.; Even, J. Entropy in halide perovskites. *Nat. Mater.* **2018**, *17*, 377.
(18) Egger, D. A.; Bera, A.; Cahen, D.; Hodes, G.; Kirchartz, T.; Kronik, L.; Lovrincic, R.; Rappe, A. M.; Reichman, D. R.; Yaffe, O. What remains unexplained about the properties of halide perovskites? *Adv. Mater.* **2018**, *30*, No. e1800691.
(19) Rivett, J. P. H.; Tan, L. Z.; Price, M. B.; Bourelle, S. A.; Davis, N. J. L. K.; Xiao, J.; Zou, Y.; Middleton, R.; Sun, B.; Rappe, A. M.; Credgington, D.; Deschler, F. Long-lived polarization memory in the electronic states of lead-halide perovskites from local structural dynamics. *Nat. Commun.* **2018**, *9*, 3531.
(20) Du, W.; Zhang, S.; Zhang, Q.; Liu, X. Recent Progress of Strong Exciton−Photon Coupling in Lead Halide Perovskites. *Adv. Mater.* **2019**, *31*, No. 1804894.
(21) Kirschner, M. S.; Diroll, B. T.; Guo, P.; Harvey, S. M.; Helweh, W.; Flanders, N. C.; Brumberg, A.; Watkins, N. E.; Leonard, A. A.; Evans, A. M.; Wasielewski, M. R.; Dichtel, W. R.; Zhang, X.; Chen, L. X.; Schaller, R. D. Photoinduced, reversible phase transitions in all-inorganic perovskite nanocrystals. *Nat. Commun.* **2019**, *10*, 504.
(22) Wu, X.; Tan, L. Z.; Shen, X.; Hu, T.; Miyata, K.; Trinh, M. T.; Li, R.; Coffee, R.; Liu, S.; Egger, D. A.; Makasyuk, I.; Zheng, Q.; Fry, A.; Robinson, J. S.; Smith, M. D.; Guzelturk, B.; Karunadasa, H. I.; Wang, X.; Zhu, X.; Kronik, L.; Rappe, A. M.; Lindenberg, A. M. Light-induced picosecond rotational disordering of the inorganic sublattice in hybrid perovskites. *Sci. Adv.* **2017**, *3*, No. e1602388.
(23) Guzelturk, B.; Winkler, T.; Van de Goor, T. W. J.; Smith, M. D.; Bourelle, S. A.; Feldmann, S.; Trigo, M.; Teitelbaum, S. W.; Steinrück, H.-G.; de la Pena, G. A.; Alonso-Mori, R.; Zhu, D.; Sato, T.; Karunadasa, H. I.; Toney, M. F.; Deschler, F.; Lindenberg, A. M. Visualization of dynamic polaronic strain fields in hybrid lead halide perovskites. *Nat. Mater.* **2021**, *20*, 618−623.
(24) Liu, C.; Wang, Y.; Geng, H.; Zhu, T.; Ertekin, E.; Gosztola, D.; Yang, S.; Huang, J.; Yang, B.; Han, K.; Canton, S. E.; Kong, Q.; Zheng, K.; Zhang, X. Asynchronous photoexcited electronic and structural relaxation in lead-free perovskites. *J. Am. Chem. Soc.* **2019**, *141*, 13074−13080.
(25) Yang, B.; Chen, J.; Hong, F.; Mao, X.; Zheng, K.; Yang, S.; Li, Y.; Pullerits, T.; Deng, W.; Han, K. Lead-Free, Air-Stable All-Inorganic Cesium Bismuth Halide Perovskite Nanocrystals. *Angew. Chem., Int. Ed.* **2017**, *56*, 12471−12475.
(26) Lindenberg, A. M.; Larsson, J.; Sokolowski-Tinten, K.; Gaffney, K.; Blome, C.; Synnergren, O.; Sheppard, J.; Caleman, C.; Macphee, A. G.; Weinstein, D.; Lowney, D. P.; Allison, T. K.; Matthews, T.; Falcone, R. W.; Cavalieri, A. L.; Fritz, D. M.; Lee, S. H.; Bucksbaum, P. H.; Reis, D. A.; Rudati, J.; Fuoss, P. H.; Kao, C. C.; Siddons, D. P.; Pahl, R.; Als-Nielsen, J.; Duesterer, S.; Ischebeck, R.; Schlarb, H.; Schulte-Schrepping, H.; Tschentscher, T.; Schneider, J.; von der Linde, D.; Hignette, O.; Sette, F.; Chapman, H. N.; Lee, R. W.; Hansen, T. N.; Techert, S.; Wark, J. S.; Bergh, M.; Huldt, G.; van der Spoel, D.; Timneanu, N.; Hajdu, J.; Akre, R. A.; Bong, E.; Krejcik, P.; Arthur, J.; Brennan, S.; Luening, K.; Hastings, J. B. Atomic-scale visualization of inertial dynamics. *Science* **2005**, *308*, 392−395.
(27) Mannebach, E. M.; Li, R.; Duerloo, K.-A.; Nyby, C.; Zalden, P.; Vecchione, T.; Ernst, F.; Reid, A. H.; Chase, T.; Shen, X.; Weathersby, S.; Hast, C.; Hettel, R.; Coffee, R.; Hartmann, N.; Fry, A. R.; Yu, Y.; Cao, L.; Heinz, T. F.; Reed, E. J.; Dürr, H. A.; Wang, X.; Lindenberg, A. M. Dynamic structural response and deformations of monolayer MoS2 visualized by femtosecond electron diffraction. *Nano Lett.* **2015**, *15*, 6889−6895.
(28) Kirschner, M. S.; Hannah, D. C.; Diroll, B. T.; Zhang, X.; Wagner, M. J.; Hayes, D.; Chang, A. Y.; Rowland, C. E.; Lethiec, C. M.; Schatz, G. C.; Chen, L. X.; Schaller, R. D. Transient Melting and Recrystallization of Semiconductor Nanocrystals Under Multiple Electron−Hole Pair Excitation. *Nano Lett.* **2017**, *17*, 5314−5320.
(29) Tsai, H.; Asadpour, R.; Blancon, J.-C.; Stoumpos, C. C.; Durand, O.; Strzalka, J. W.; Chen, B.; Verduzco, R.; Ajayan, P. M.; Tretiak, S.; Even, J.; Alam, M. A.; Kanatzidis, M. G.; Nie, W.; Mohite, A. D. Light-induced lattice expansion leads to high-efficiency perovskite solar cells. *Science* **2018**, *360*, 67−70.

https://doi.org/10.1021/jacs.1c11747
J. Am. Chem. Soc. 2022, 144, 5335−5341

(30) Izumi, F.; Ikeda, T. Implementation of the Williamson-Hall and Halder-Wagner Methods into RIETAN-FP. In *Annual report Advanced Ceramics Research Center Nagoya Institute of Technology*, 2015; vol. *3*, pp. 33−38.
(31) Wong, W. P.; Yin, J.; Chaudhary, B.; Chin, X. Y.; Cortecchia, D.; Lo, S.-Z. A.; Grimsdale, A. C.; Mohammed, O. F.; Lanzani, G.; Soci, C. Large polaron self-trapped states in three-dimensional metal-halide perovskites. *ACS Mater. Lett.* **2019**, *2*, 20−27.
(32) Yang, B.; Han, K. Ultrafast Dynamics of Self-Trapped Excitons in Lead-Free Perovskite Nanocrystals. *J. Phys. Chem. Lett.* **2021**, *12*, 8256−8262.
(33) Nishida, J.; Breen, J. P.; Lindquist, K. P.; Umeyama, D.; Karunadasa, H. I.; Fayer, M. D. Dynamically Disordered Lattice in a Layered Pb-I-SCN Perovskite Thin Film Probed by Two-Dimensional Infrared Spectroscopy. *J. Am. Chem. Soc.* **2018**, *140*, 9882−9890.
(34) Park, M.; Neukirch, A. J.; Reyes-Lillo, S. E.; Lai, M.; Ellis, S. R.; Dietze, D.; Neaton, J. B.; Yang, P.; Tretiak, S.; Mathies, R. A. Excited-state vibrational dynamics toward the polaron in methylammonium lead iodide perovskite. *Nat. Commun.* **2018**, *9*, 2525.
(35) Sundaram, S. K.; Mazur, E. Inducing and probing non-thermal transitions in semiconductors using femtosecond laser pulses. *Nat. Mater.* **2002**, *1*, 217−224.
(36) Buizza, L. R.; Herz, L. M. Polarons and Charge Localization in Metal-Halide Semiconductors for Photovoltaic and Light-Emitting Devices. *Adv. Mater.* **2021**, *33*, No. 2007057.
(37) McCall, K. M.; Stoumpos, C. C.; Kostina, S. S.; Kanatzidis, M. G.; Wessels, B. W. Strong electron−phonon coupling and self-trapped excitons in the defect halide perovskites A3M2I9 (A= Cs, Rb; M= Bi, Sb). *Chem. Mater.* **2017**, *29*, 4129−4145.
(38) Tailor, N. K.; Maity, P.; Satapathi, S. Observation of Negative Photoconductivity in Lead-Free Cs3Bi2Br9Perovskite Single Crystal. *ACS Photonics* **2021**, *8*, 2473−2480.
(39) Ghosh, B.; Wu, B.; Mulmudi, H. K.; Guet, C.; Weber, K.; Sum, T. C.; Mhaisalkar, S.; Mathews, N. Limitations of Cs3Bi2I9 as Lead-Free Photovoltaic Absorber Materials. *ACS Appl. Mater. Interfaces* **2018**, *10*, 35000−35007.
(40) Han, T.-R. T.; Zhou, F.; Malliakas, C. D.; Duxbury, P. M.; Mahanti, S. D.; Kanatzidis, M. G.; Ruan, C.-Y. Exploration of metastability and hidden phases in correlated electron crystals visualized by femtosecond optical doping and electron crystallography. *Sci. Adv.* **2015**, *1*, No. e1400173.
(41) Wall, S.; Yang, S.; Vidas, L.; Chollet, M.; Glownia, J. M.; Kozina, M.; Katayama, T.; Henighan, T.; Jiang, M.; Miller, T. A.; Reis, D. A.; Boatner, L. A.; Delaire, O.; Trigo, M. Ultrafast disordering of vanadium dimers in photoexcited VO₂. *Science* **2018**, *362*, 572−576.
(42) Ahmad, M.; Rehman, G.; Ali, L.; Shafiq, M.; Iqbal, R.; Ahmad, R.; Khan, T.; Jalali-Asadabadi, S.; Maqbool, M.; Ahmad, I. Structural, electronic and optical properties of CsPbX3 (X=Cl, Br, I) for energy storage and hybrid solar cell applications. *J. Alloys Compd.* **2017**, *705*, 828−839.
(43) Xue, J.; Yang, D.; Cai, B.; Xu, X.; Wang, J.; Ma, H.; Yu, X.; Yuan, G.; Zou, Y.; Song, J.; Zeng, H. Photon-Induced Reversible Phase Transition in CsPbBr3 Perovskite. *Adv. Funct. Mater.* **2019**, *29*, No. 1807922.
(44) Blancon, J. C.; Stier, A. V.; Tsai, H.; Nie, W.; Stoumpos, C. C.; Traoré, B.; Pedesseau, L.; Kepenekian, M.; Katsutani, F.; Noe, G. T.; Kono, J.; Tretiak, S.; Crooker, S. A.; Katan, C.; Kanatzidis, M. G.; Crochet, J. J.; Even, J.; Mohite, A. D. Scaling law for excitons in 2D perovskite quantum wells. *Nat. Commun.* **2018**, *9*, 2254.
(45) Ke, W.; Kanatzidis, M. G. Prospects for low-toxicity lead-free perovskite solar cells. *Nat. Commun.* **2019**, *10*, 965.
(46) Jones, T. W.; Osherov, A.; Alsari, M.; Sponseller, M.; Duck, B. C.; Jung, Y.-K.; Settens, C.; Niroui, F.; Brenes, R.; Stan, C. V.; Li, Y.; Abdi-Jalebi, M.; Tamura, N.; Macdonald, J. E.; Burghammer, M.; Friend, R. H.; Bulović, V.; Walsh, A.; Wilson, G. J.; Lilliu, S.; Stranks, S. D. Lattice strain causes non-radiative losses in halide perovskites. *Energy Environ. Sci.* **2019**, *12*, 596−606.

https://doi.org/10.1021/jacs.1c11747
J. Am. Chem. Soc. 2022, 144, 5335−5341